ELECTROCHEMISTRY

La- and Mn-doped cobalt spinel oxygen evolution catalyst for proton exchange membrane electrolysis

Lina Chong[1], Guoping Gao[2], Jianguo Wen[3], Haixia Li[2], Haiping Xu[1], Zach Green[4], Joshua D. Sugar[5], A. Jeremy Kropf[1], Wenqian Xu[6], Xiao-Min Lin[3], Hui Xu[4], Lin-Wang Wang[2], Di-Jia Liu[1,7]*

Discovery of earth-abundant electrocatalysts to replace iridium for the oxygen evolution reaction (OER) in a proton exchange membrane water electrolyzer (PEMWE) represents a critical step in reducing the cost for green hydrogen production. We report a nanofibrous cobalt spinel catalyst codoped with lanthanum (La) and manganese (Mn) prepared from a zeolitic imidazolate framework embedded in electrospun polymer fiber. The catalyst demonstrated a low overpotential of 353 millivolts at 10 milliamperes per square centimeter and a low degradation for OER over 360 hours in acidic electrolyte. A PEMWE containing this catalyst at the anode demonstrated a current density of 2000 milliamperes per square centimeter at 2.47 volts (Nafion 115 membrane) or 4000 milliamperes per square centimeter at 3.00 volts (Nafion 212 membrane) and low degradation in an accelerated stress test.

L ow-temperature water electrolysis can rapidly produce environmentally sustainable, or green, hydrogen and is a prospective means of storing energy from renewable but intermittent power sources, such as wind and solar, in future clean energy infrastructure (1–4). Commercial systems use either liquid alkaline electrolyte or proton exchange membrane electrolyte (1). Compared with the alkaline counterpart, a proton exchange membrane water electrolyzer (PEMWE) offers the advantages of higher current density, higher H_2 purity, lower resistance losses, and more compact design, rendering it a preferred technology where high efficiency and small footprint are essential (1, 2). Working under the acidic and oxidative environment, however, adds substantial challenges to the catalyst activity and stability profile. This is particularly the case for the anode catalyst because of the high overpotential for oxygen evolution reaction (OER) (3). At present, OER catalysts for PEMWE are primarily restricted to the platinum group metal (PGM) materials, such as IrO_x (1). Their high cost and limited reserve, however, pose substantial barriers to the widespread implementation of PEMWE. Low-cost transition metals and their oxides are known to be active toward OER in alkaline electrolyte (4–6), but their demonstration in acidic electrolyte is very limited (1, 7, 8).

Cobalt molecular and oxide compounds have emerged as promising OER catalysts for water

splitting in recent years (9). Kanan and Nocera systematically investigated water oxidation using a catalyst deposited from Co^{2+} solution in pH 7 phosphate buffer (10). Gerken et al. performed a comprehensive mechanistic study of cobalt-catalyzed water oxidation from homogeneous to heterogeneous phases in electrolyte over a broad pH range of 0 to 14 (11). Those studies have provided profound understanding of electrocatalytic oxygen evolution by cobalt. More recently, thin film spinel-type Co_3O_4 was found to be active toward OER and stable at low overpotential in acid (12). The activity and stability of Co oxide were improved substantially when modified with iron, manganese, antimonite, and PbO_x (13–15). In addition to activity and stability, the inherent conductivity represents an essential requirement for efficient OER electrocatalysis to overcome the insulating properties of most transition metal oxides in their crystalline form. Conventional carbon supports, used to facilitate the electron conductivity, are not stable against oxidation to CO_2 at the PEMWE anode under OER operating potential. For example, a Co-polyoxometalate composited with carbon paste achieved a lower OER onset potential than IrO_2 in 1 M sulfuric acid but decayed quickly, presumably as a result of oxidative corrosion of the carbon (16). Self-conductive oxide catalysts can also enhance the active-site volumetric density without being diluted by a secondary nonactive support. A recently developed self-healing OER catalyst has demonstrated excellent activity and durability in acidic electrolyte (14). The approach, however, requires the presence of metal precursors in the aqueous electrolyte, hindering integration into a PEMWE. Most of the aforementioned studies were carried out either in half-cells or aqueous electrolyzers, where the demands for OER catalyst stability and conductivity are different from those in a PEMWE. For example, the dissolved transition metal concentra-

tion must be minimized to avoid poisoning proton exchange membrane in the PEMWE. Effective OER for PEMWE requires optimal interfacial properties, microporosity, and surface catalytic activity (1), all of which need to be validated in the operating electrolyzer.

In this work, we present a cobalt spinel–based OER catalyst derived from a zeolitic methyl-imidazolate framework (Co-ZIF) and processed by electrospinning. The catalyst demonstrated excellent OER activity benefiting from its high specific surface area, porous interconnected nanonetwork structure, and high conductivity.

Design of an acid-stable cobalt OER catalyst

Our design concept of an efficient cobalt spinel–based OER catalyst for PEMWE anodes is based on the following rationale: To enhance OER activity in acid, an oversized and more stable second element can be selectively introduced to the cobalt oxide surface to generate strain, oxygen vacancy (V_o), and acid tolerance (17); to improve the oxide electronic conductivity, a third element with similar charge and dimension to cobalt may be incorporated inside the lattice to bridge the Fermi bandgap through d orbital partial occupation of the third element induced by its d-electron delocalization. Advancing further from the rotating disk electrode (RDE) or half-cell study to a membrane electrode assembly (MEA) demonstration, the catalyst should have a high porosity and surface area easily accessible to the reactant (H_2O). Meanwhile, the electrode layer should be effective in transporting H_2O and releasing O_2 without blocking the water-catalyst interface. Furthermore, the oxide catalyst should be self-conductive without the need for another conductive support, such as carbon, that is unstable under high OER operating potential and current density. Finally, the metal oxide should be stable against oxidative and acidic (pH 2 to 4) corrosion in the PEMWE environment.

We selected Co-ZIF as the precursor for the catalyst preparation because of its high intrinsic porosity and reticular structure. It has recently been used to prepare a nanoplate oxide with excellent OER activity tested in strong alkaline electrolyte (1 M KOH) using the RDE method (18). Our catalyst preparation through low-temperature oxidation partially retained the porosity and morphology of Co-ZIFs after their conversion into interconnected hollow metal oxide particles, providing an excellent platform for enhanced charge and mass transfer. Among different elements that we screened, we selected lanthanum (La^{3+}) as the second element because of its much larger radius compared with that of Co^{2+} (1.06 Å versus 0.72 Å) along with its strong affinity to bind –OH groups at the surface of cobalt oxide. We also added manganese ions (Mn^{2+}) of similar

[1]Chemical Science and Engineering Division, Argonne National Laboratory, Lemont, IL 60439, USA. [2]Material Science Division, Lawrence Berkeley National Laboratory, Berkeley, CA 94720, USA. [3]Center for Nanoscale Materials, Argonne National Laboratory, Lemont, IL 60439, USA. [4]Giner Inc., Auburndale, MA 02466, USA. [5]Sandia National Laboratory, Livermore, CA 94550, USA. [6]X-ray Science Division, Advanced Photon Source, Argonne National Laboratory, Lemont, IL 60439, USA. [7]Pritzker School of Molecular Engineering, University of Chicago, Chicago, IL 60637, USA.
*Corresponding author. Email: djliu@anl.gov
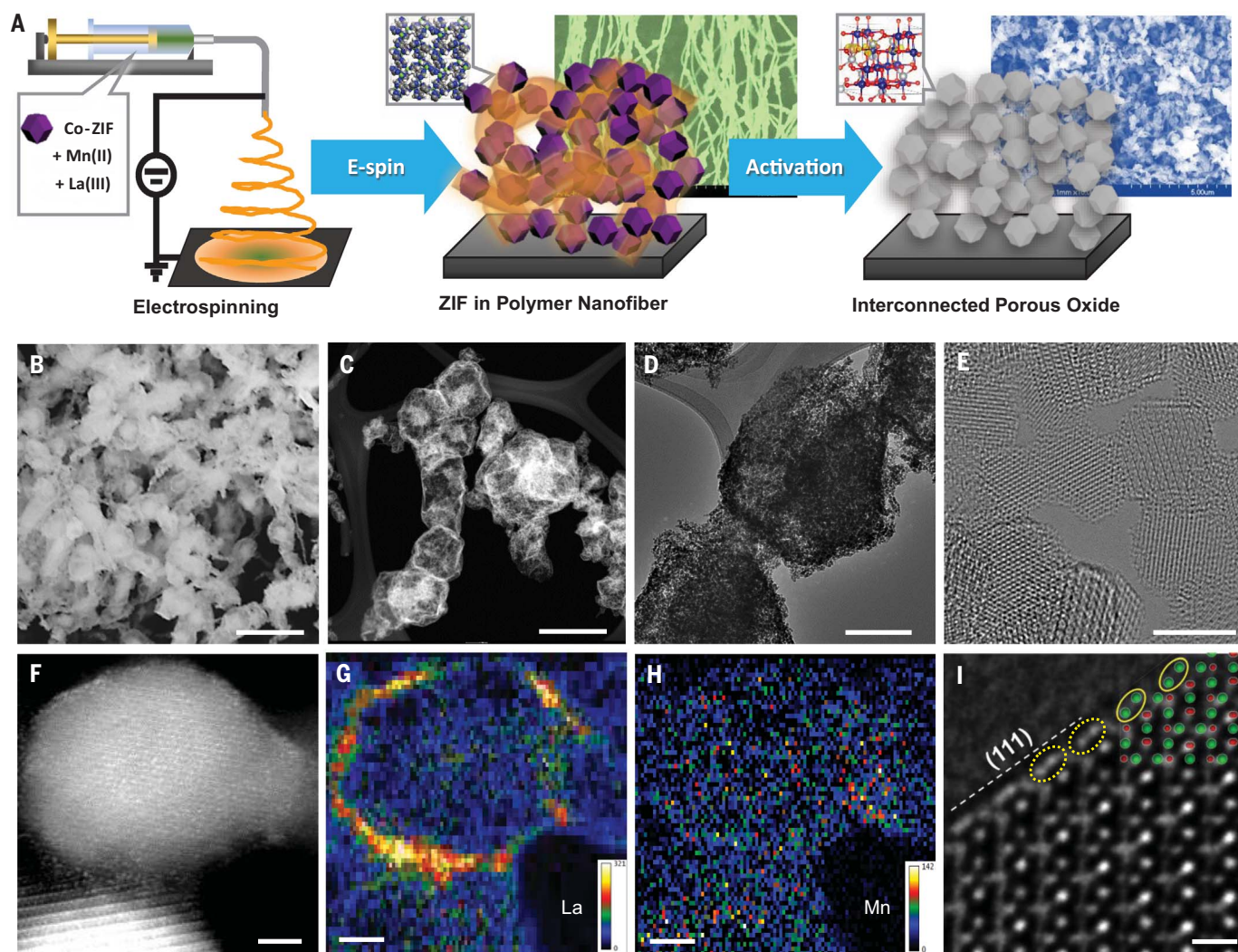
Fig. 1. Synthesis, morphology, and structure of LMCF. (**A**) Schematics of LMCF synthesis including formation of Co-ZIF embedded PAN polymer fiber by electrospinning and thermal oxidative activation to produce interconnected porous cobalt oxide particles after removing all the organics. The background SEM images show a cross-linked, ZIF-containing fiber nanonetwork produced by electrospinning and the interconnected porous oxide after the activation. (**B**) SEM image (scale bar, 1 μm). (**C**) HAADF-STEM image (scale bar, 500 nm). (**D**) TEM image (scale bar, 200 nm). (**E**) HRTEM image (scale bar, 5 nm).

(**F** to **H**) STEM image and the corresponding La and Mn distributions (scale bar, 2 nm). The color bars show the element counts. The maximal counts are 321 for La and 142 for Mn. (**I**) HRTEM image (scale bar, 0.5 nm). The green dots represent atomic columns of tetrahedral (T) and octahedral (O) oxygens, and the red dots represent the cobalt atomic columns simulated based on bulk phase inside lattice. The dotted yellow ellipses (on surface) show a different orientation compared with the solid yellow ellipses from the simulation (in bulk), suggesting a shift of oxygen position as a result of lattice relaxation.

radius to Co^{2+} (0.8 Å versus 0.72 Å) during the Co-ZIF synthesis, which would be oxidized to Mn^{3+} (0.72 Å) during the oxidative conversion and uniformly distributed inside the cobalt spinel lattice to promote conductivity (via bandgap) and OER activity (via affinity OH or H group). The catalyst synthesis scheme is shown in Fig. 1A. Briefly, La- and Mn-doped Co-ZIF, LaMn@Co-ZIF, was prepared in solution. Powder x-ray diffraction (XRD) combined with scanning electron microscopy (SEM)–energy dispersive x-ray spectroscopy (EDX) elemental mapping confirmed the successful incorporation of atomic La and Mn into the structure and cavity of the Co-ZIF (fig. S1).

The LaMn@Co-ZIF was then suspended in a polyacrylonitrile (PAN) polymer slurry (LaMn@Co-ZIF/PAN) (19), which was subsequently electrospun into a fibrous mat. The nanofiber embedded with individual LaMn@Co-ZIF was activated in flowing air at 360°C for 6 hours to remove the organic components, forming La- and Mn-codoped porous cobalt spinel fibers (denoted LMCF). Thermogravimetric analysis (TGA) confirmed the removal of carbon and nitrogen in LMCF after oxidative activation (fig. S2). The SEM image of LMCF shows an interconnected nanofibrous network morphology with ample macropores in between the entwined nanofibers (Fig. 1B). High-angle

annular dark-field scanning transmission electron microscopy (HAADF-STEM) revealed that individual LMCF particles retained the original Co-ZIF's rhombic dodecahedral shape, aligned and fused together in strings after oxidation (Fig. 1C). The ZIF-shaped LMCF particle is highly porous with a hollow structure composed of nanopores, as shown by transmission electron microscopy (TEM) (Fig. 1D). Each particle is composed of aggregates of Co_3O_4 nanocrystallites, with an average size of ~3.5 nm, determined by aberration-corrected high-resolution transmission electron microscopy (HRTEM) (Fig. 1E and fig. S3). Nitrogen adsorption measurement of LMCF at 77 K
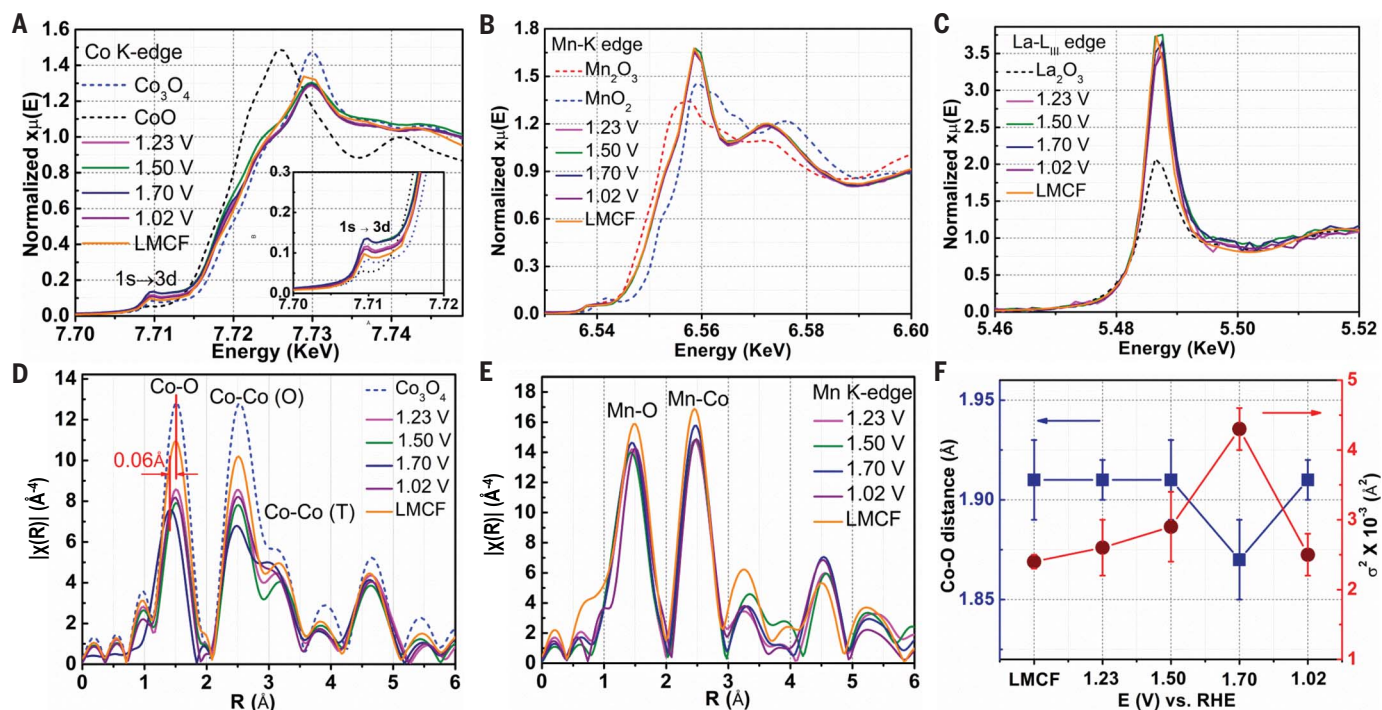
Fig. 2. XAS study of LMCF. (A to **C)** Fluorescence XANES spectra collected at Co K-edge (A) (inset: enlarged pre-edge 1s → 3d transition), Mn K-edge (B), and La L$_{III}$-edge (C) under ex situ (LMCF) and operando conditions at different potentials. Co$_3$O$_4$, CoO, Mn$_2$O$_3$, MnO$_2$, and La$_2$O$_3$ are used as the references. (**D** and **E**) R-space EXAFS spectra at Co K-edge (D) and Mn K-edge (E) of the same samples. (**F**) Co-O bond distances (blue line) and DWF (red line) surround Co derived from EXAFS data taken at different cell potentials. Error bars represent the uncertainty of Fourier transformation of the experimental EXAFS data.

provided a Brunauer–Emmett–Teller (BET) specific surface area (SSA) of 197 m^2 g^{-1} and a pore volume of 0.463 cm^3 g^{-1} (fig. S4). The high porosity of individual LMCF particle combined with nanofibrous morphology improves accessibility of reactants to the catalytic sites and facilitates water-oxygen mass transport in and out of the catalyst structure—an essential attribute for high-OER current density. XRD and Raman spectroscopy confirmed that the catalyst exhibited a spinel Co$_3$O$_4$ structure of slightly expanded lattice and higher Co^{2+}/Co^{3+} ratio (fig. S5C and table S1). STEM images showed that the individual crystal surface is dominated by (111) facets, and electron energy-loss spectroscopy (EELS) elemental mapping revealed La localization on the surface, with Mn distributed mainly in the bulk (Fig. 1, F to H, and fig. S6). Low-magnification EDX elemental mapping disclosed a uniform distribution of Co, Mn, La, and O in LMCF, and inductively coupled plasma optical emission spectrometry (ICP-OES) determined an atomic ratio of Co:Mn:La of 80:12:8 (fig. S7 and table S3). HRTEM imaging revealed that the LMCF lattice surface was terminated by oxygen atoms in a relaxed state, with positions shifted from those inside the crystallite (20) due to V_o (Fig. 1I and fig. S8), an important attribute in lowering the OER activation energy and stabilizing the intermediate during the reaction (17, 21). We also measured LMCF conductivity

using the four-probe van der Pauw method for comparison with IrO$_x$ and commercial Co$_3$O$_4$. The LMCF conductivity was found to be 8.6 times as high as that of commercial Co$_3$O$_4$ and about two-thirds that of IrO$_x$ (fig. S9).

The electronic configuration and the coordination structure of Co, La, and Mn in LMCF were investigated using x-ray photoelectron spectroscopy (XPS) (fig. S10A and table S4) and synchrotron x-ray absorption spectroscopy (XAS). The high-resolution O 1s XPS spectrum confirmed the presence of high V_o concentration in LMCF (fig. S11A). The Co 2p XPS spectrum revealed a higher ratio of Co^{2+}:Co^{3+} in LMCF compared with that in Co$_3$O$_4$ (fig. S11B). The x-ray absorption near-edge structure (XANES) spectrum at the Co K-edge (LMCF) shows a very similar spectral pattern to that of Co$_3$O$_4$ with a slightly red-shifted absorption energy and a decreased white line (WL) intensity (Fig. 2A), indicating a lower average oxidation state and a smaller O coordination number (CN) to cobalt in LMCF, which agrees well with the Raman and XPS results. We also observed an enhanced 1s → 3d transition peak intensity, which reveals that the cobalt in LMCF is in a less centrosymmetric coordination environment than that in Co$_3$O$_4$, suggesting a distorted Co oxide lattice by V_o. Compared with Co$_3$O$_4$, the LMCF extended x-ray absorption fine structure (EXAFS) shows lower peak intensities and CNs corresponding

to Co-O and Co-Co shells (Fig. 2D, fig. S12, and table S5), which further supports a less developed lattice with a high concentration of V_o from smaller particle size and higher Co^{2+} (tetrahedral O-coordinated) fraction in LMCF. XANES at the Mn K-edge indicates that the average manganese oxidation state is between +3 and +4 (Fig. 2B). Both K-space and R-space spectra extracted from EXAFS exhibit significant differences from that in Mn oxide references (Mn$_3$O$_4$, Mn$_2$O$_3$, and MnO$_2$) (fig. S13, B and C). R-space fitting determined the CNs of Mn to O and Mn to Co to be 5.5 ± 0.4 and 7.2 ± 0.3, respectively (table S5). Most noticeably, the first and second shell radii and CNs are close to those of Co-O and Co-Co$_{(oh)}$ in Co$_3$O$_4$ (Fig. 2E and tables S5 and S6) instead of Mn-O and Mn-Mn paths in Mn references, including Mn$_3$O$_4$, Mn$_2$O$_3$, and MnO$_2$ (fig. S13B). These observations provide convincing evidence that the Mn substitutes for the Co^{3+} at the edge-sharing octahedral site and is embedded inside the cobalt oxide matrix in LMCF, in agreement with the HAADF-STEM result. The Mn^{3+} in the lattice is known to enhance OER activity of the oxide in acid (22). The XANES spectrum of La in LMCF shows significantly higher WL intensity than that of the La$_2$O$_3$ reference (Fig. 2C). Given that the WL intensity for oxides is generally proportional to the number of coordinated oxygens, R-space fitting determined the CN

of La to oxygen in LMCF to be 8.3, which is in between that of lanthanum oxide (CN = 6) and hydroxide (CN = 9) (fig. S14).

Electrocatalytic activity in solution

We first evaluated the OER catalytic activity of LMCF using the RDE method in 0.1 M HClO$_4$ electrolyte (pH = 1). To better understand the effects of the second and third elemental doping, we also prepared Co$_3$O$_4$ fiber (CF)

and La-doped Co$_3$O$_4$ fiber (LCF) using a similar Co-ZIF–electrospinning method. Commercial Co$_3$O$_4$ and Ir black were also studied as benchmarks. Figure 3A shows a progressive improvement of OER activity measured by cyclic voltammogram (CV) through the addition of Mn and La in CF. The performance of LMCF also significantly exceeds that of commercial Co$_3$O$_4$ and approaches that of Ir black. Figure 3B presents the mass activity

(MA) Tafel plot for LMCF together with the benchmark samples. LMCF again exhibits a high intrinsic catalytic activity. For example, LMCF catalyst shows a bulk MA of 126 ± 20 A g^{-1} at an overpotential of 370 mV, which is higher than that of commercial Ir black (table S7). This is possibly because of a higher gravimetric catalytic site density of LMCF due to its lower molecular weight compared with IrO$_x$. LMCF evaluated by linear sweep
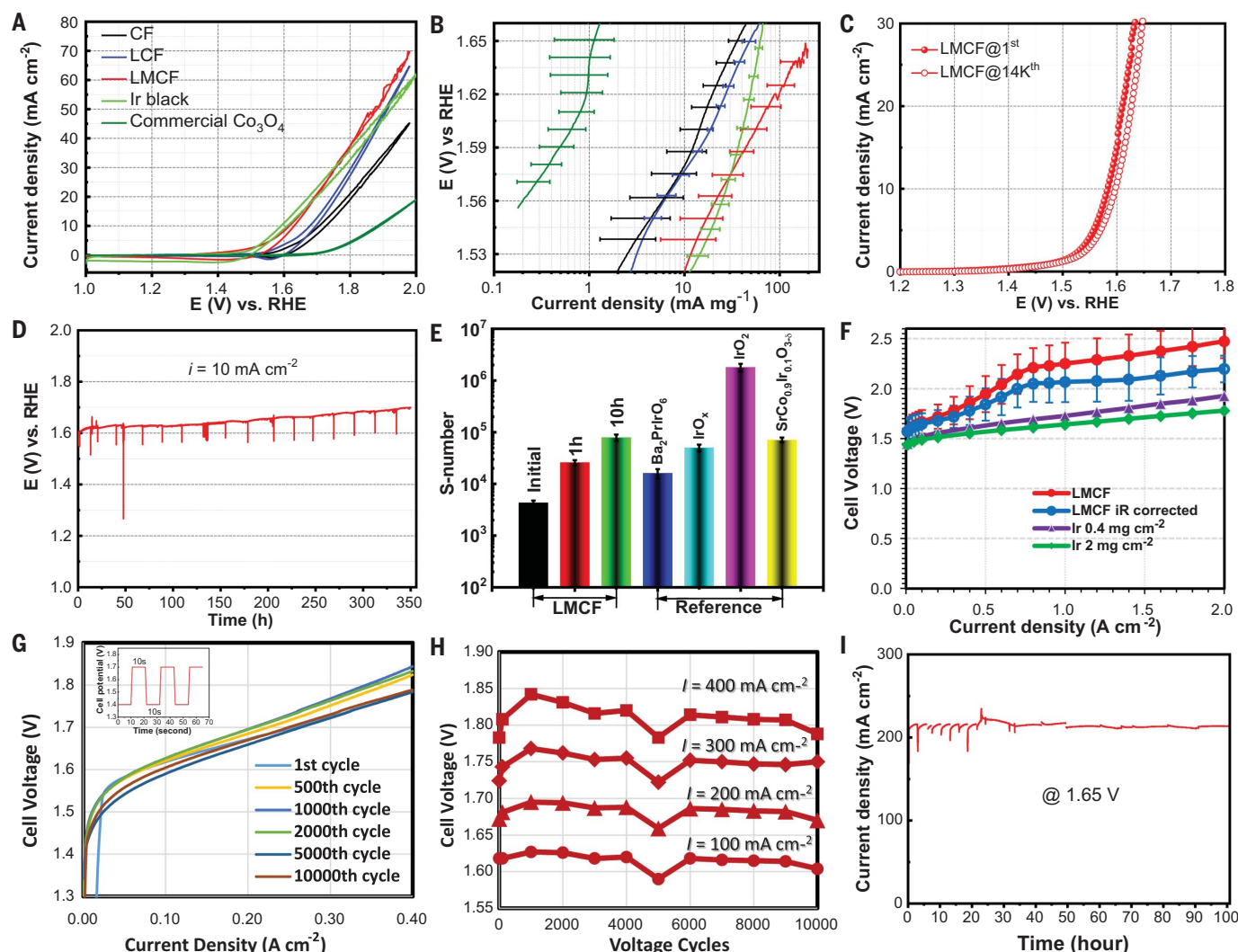
Fig. 3. Electrocatalytic performance of LMCF. (**A**) CVs of LMCF, LCF, CF, Ir black, and commercial Co$_3$O$_4$ in O$_2$-saturated 0.1 M HClO$_4$ (PGM-free catalyst loadings = ~260 ± 30 μg cm^{-2}, Ir black loading = ~230 ± 30 μg cm^{-2}). (**B**) Tafel plots of LMCF, LCF, CF, Ir black, and commercial Co$_3$O$_4$, with error bars of one standard deviation over four experimental replicates. (**C**) LSVs of LMCF measured by RDE before and after 14,000 voltage cycles in O$_2$-saturated 0.1 M HClO$_4$ (with 95% *iR* correction). (**D**) Chronopotentiometric response at 10 mA cm^{-2} with LMCF catalyst loading of 0.9 mg cm^{-2} over 353-hour test. (**E**) *S* number calculated for LMCF after different hours onstream compared with selected benchmark Ir-based catalysts. (**F**) Current-voltage polarizations (*iR* corrected and uncorrected) of the PEMWE cell with LMCF anodic catalyst compared with that of Ir black catalysts with different loadings at 80°C. The

polarization plot for LMCF represents an average of three MEA measurements with one standard deviation. (**G**) Current-voltage polarizations of the PEMWE after selected cycle numbers during a multiple-voltage cycling AST. The inset shows the stepwise voltage swing between 1.4 V and 1.7 V with 10-s dwell time at each potential. (**H**) PEMWE cell voltage measured at different current densities after selected voltage cycles during the AST. (**I**) Potentiostatic measurement of PEMWE at the cell potential of 1.65 V for LMCF anodic catalyst over 100 hours. Test conditions: anode LMCF catalyst loading, 1 to 2 mg cm^{-2}; cathode Pt loading, 0.4 mg$_{Pt}$ cm^{-2}; 60° or 80°C cell temperature, unless otherwise specified; 5-cm^2 active electrode area; Nafion 115 membrane for (F), (G), and (H), and Nafion 212 membrane for (I); DI water at flow rate of 10 ml min^{-1}.

voltammetry (LSV) (Fig. 3C, with 95% *iR* correction) shows an onset potential of 1.28 V measured at 0.46 mA cm^{-2} and an overpotential of 353 ± 30 mV at 10 mA cm^{-2}. The LMCF catalyst activity was also measured in 0.5 M H$_2$SO$_4$ (pH = 0), and the overpotential was reduced to 335 ± 30 mV at 10 mA cm^{-2} (fig. S15). These results placed LMCF among the most active PGM-free catalysts reported in aqueous acid (*23*) (table S2). We estimated the electrochemical surface areas (ECSA) of the catalysts by measuring the double-layer capacitance from the CV curves in the non-Faradaic region (fig. S16) and produced Tafel plots of the ECSA-based specific current densities (fig. S17). The intrinsic activities of LMCF were further assessed based on turnover frequencies (TOFs) at different overpotentials (320 mV, 370 mV, and 650 mV), which are among the highest when compared with representative PGM-free and PGM OER catalysts tested in various acidic media (table S8). For example, the TOF of LMCF is calculated to be 0.079 ± 0.011 s^{-1} at an overpotential of 370 mV based on the total loading mass, which increases to 0.87 ± 0.09 s^{-1} when calculated based on ECSA (table S7). We also analyzed O$_2$ produced during OER over LMCF in a H cell using in situ gas chromatography (GC) and calculated the Faradaic efficiencies (FEs) for the oxygen produced at the current densities of 10 mA cm^{-2}, 20 mA cm^{-2}, 30 mA cm^{-2}, and 50 mA cm^{-2} (fig. S18, A to C). An average FE of 99.3 ± 5% was obtained, indicating that the oxygen formation through the four-electron transfer during water splitting is the only electrochemical reaction over LMCF. Ir was measured as reference, for which the FE was 97.0 ± 5% (fig. S18C).

LMCF was subjected to an accelerated aging test through voltage cycling between 1.4 V and 2.0 V versus reversible hydrogen electrode (RHE) by RDE in 0.1 M HClO$_4$ electrolyte. A mere ~20-mV potential loss at 10 mA cm^{-2} was observed after 14,000 CV cycles (Fig. 3C). Such stability was found to be better than that of commercial Co$_3$O$_4$ or Ir black at comparable catalyst weight loadings (fig. S19). The morphology, composition, and electronic states of the LMCF after the voltage cycling were found to be nearly unchanged from the pristine state (fig. S20, A to E). Similarly, no appreciable changes in the XANES spectra of Co, Mn, and La were observed after the voltage cycling (fig. S20, F to H). We further tested LMCF galvanostatic stability by holding the electrode current density at 10 mA cm^{-2} for an extended operation period, following a test protocol (*23*, *24*) (Fig. 3D). The change of electrode potential in acidic electrolyte was monitored over 353 hours, and a slow degradation at an average rate of 0.28 mV hour^{-1} was observed. Transient potential dips in Fig. 3D were the result of pauses of the measurement

while the electrolyte was refreshed. We also checked the metal contents in the electrolyte from acid leaching by performing ICP-OES under OER electrocatalysis. A mild loss of Co, Mn, and La ions by ~1.9 wt %, ~2.8 wt %, and ~1.1 wt % over their stoichiometric loadings in the LMCF catalyst, respectively, in a period of 80 hours was observed during the chronopotentiometry at 10 mA cm^{-2} (fig. S21A). After an initial jump at the first hour, the metal dissolution rate decreased markedly afterward. Meanwhile, the catalytic activity remained nearly the same, which suggests that the dissolved metals could be attributed mainly to some loosely bound oxides at the surface. We also calculated the stability number (*S* number) for LMCF based on the amount of Co dissolved in the electrolyte at different testing times using the framework proposed by Geiger *et al.* (*25*) as well as the activity-stability factor (ASF) by Kim *et al.* (*26*). These values are compared with some of the Ir-based benchmarks in the literature, and the LMCF stability was found to be comparable to some less-stable Ir materials (Fig. 3E and fig. S21B).

Electrocatalytic activity in a PEMWE

The ultimate test of an OER catalyst is its performance in the operating PEMWE. Key properties, such as porosity, stability, and conductivity, become more important for the catalyst performance under the electrolyzer working conditions in comparison with the less-strenuous RDE measurements. The LMCF was assembled into the anode of a PEMWE single cell and tested using deionized (DI) water as the feed. Figure 3F shows composite current-voltage polarization curves derived from three measurements in the PEMWE. The electrolyzer reached a current density of 2000 mA cm^{-2} at a voltage of 2.47 V (2.20 V after cell *iR* correction), which could be further reduced to 2.30 V by switching the membrane from Nafion 115 to Nafion 212, and reached a current density of 4000 ± 200 mA cm^{-2} at 3.0 V (fig. S22). In comparison, PEMWEs with Ir loading at 0.4 mg$_{Ir}$ cm^{-2} and 2.0 mg$_{Ir}$ cm^{-2} at the anode displayed cell voltages of 1.93 V and 1.78 V at 2000 mA cm^{-2} before *iR* correction, respectively. Comparisons with other reported anodic catalysts are given in table S2 (*14–16*).

The MEA with LCMF was also subjected to accelerated stress tests (ASTs) using voltage cycling, galvanostatic, and potentiostatic methods. In the voltage cycling test, the PEMWE cell voltage was swept between 1.4 V and 1.7 V with a 10-s dwell time at each voltage (square-wave) up to 10,000 cycles. Current-voltage polarization was recorded periodically after designated voltage cycles. Figure 3G shows the polarization curves recorded after the selected voltage cycles. Figure 3H demonstrates the *iR*-corrected PEMWE cell voltages at four different current

densities (100 mA cm^{-2}, 200 mA cm^{-2}, 300 mA cm^{-2}, and 400 mA cm^{-2}) after each designated cycle number taken from the tests in Fig. 3G. Only small fluctuations in the cell voltage were observed between the first and the 10,000th cycles, suggesting excellent catalyst stability under such cycling conditions. After the voltage cycling, we conducted a galvanostatic test on the same MEA at incrementally increased current densities of 50 mA cm^{-2}, 100 mA cm^{-2}, 200 mA cm^{-2}, and 300 mA cm^{-2} over a 90-hour time span (fig. S23). The cell voltages remained nearly constant after each incremental increase of the cell current until the last 10 hours, when an increasing cell voltage was observed after the current density was raised to 300 mA cm^{-2}. We also conducted a separate potentiostatic test over another PEMWE with LMCF anodic catalyst at a cell potential of 1.65 V for 100 hours (Fig. 3I). A constant cell current density of ~210 mA cm^{-2} was observed, and the anodic effluent from the PEMWE was analyzed by ICP-MS. The cobalt dissolution gradually leveled off during the first 10 hours and became negligible thereafter (fig. S24). The *S* number calculated based on the dissolution rate was found to be two orders of magnitude higher than that obtained from RDE (fig. S25A). The difference may be ascribed to the higher acidity of the electrolyte used in the RDE (pH = 1) relative to that at the MEA anode layer (pH = 2 to 4). A similar phenomenon was found in the study of RuO$_2$ catalyzed water oxidation (*25*). The lifetime determined by the *S* number suggests excellent durability of LMCF operated at the PEMWE (fig. S25B). The morphology and the surface structure of the catalyst were preserved after AST by RDE as well as by combined voltage cycling and galvanostatic tests in the PEMWE (fig. S26).

Active-site analysis

To understand the nature of the active site and the impact of the second and third metal doping, we performed in situ XAS of LMCF in an O$_2$-saturated electrolysis cell (0.1 M HClO$_4$) at the Co, Mn K-edge, and La-L$_{III}$ edge. Figure 2A shows the XANES spectra at the Co K-edge under different OER operating potentials. At the onset potential of 1.23 V when OER has yet to commence, XANES already shows a decrease in WL intensity and an increase in pre-edge 1s $\rightarrow$ 3d peak intensity compared with the spectrum of as-prepared LMCF, accompanied by a decrease of CN of the first Co-O shell (Fig. 2D, fig. S12, and table S5). This signals oxygen loss and structural change as a result of interaction with the acidic electrolyte under the electric field, altering cobalt's centrosymmetric coordination (symmetry breakdown) and electronic structure (*27*). The CN is significantly lower than that in Co$_3$O$_4$, indicating a higher fraction of tetrahedral coordinated Co^{2+} combined with higher concentration of V_O, which serves

as the nucleophilic site in promoting O–O bond formation (*28*). As the cell potential increases to initiate OER, the 1s → 3d transition becomes more intense (Fig. 2A, inset). The average valence state of cobalt in LMCF was maintained at a lower value than that of Co_3O_4 (+2.67) under all the test potentials from +2.51 at 1.02 V to +2.32 at 1.70 V (*29*) (fig. S27). Simultaneously, Fourier transformation of EXAFS spectra shows the reduction of Co-O and Co-Co shell intensities (Fig. 2D). At a potential of 1.7 V when the OER reaction proceeds much more rapidly, XAS analysis shows shortening of the Co-O bond length (Fig. 2F and table S5), indicating a high degree of covalency contraction, which positively affects the catalytic activity of the nanoparticles (*28*). A similar phenomenon was observed in an MnO_2 film, where the Mn-O bond was shortened concomitant with accumulation of Mn^{3+} and V_o under applied potential in acid (*22*). Shortened Co-O bonds during OER were

also found in the amorphous cobalt oxide OER catalyst (CoCat) (*30*), except that Co was in the +4 state, distinct from our catalyst. Accompanying the rapid acceleration of OER at 1.7 V, a clear increase of the Debye–Waller factor (DWF) σ^2 was also observed. DWF pertains to the motion of the coordinated atoms. In this case, it indicates increased Co-O vibration as the adsorbed H_2O is converted to O_2, possibly involving the shuffling lattice oxygen in LMCF, as was recently observed in a perovskite OER catalyst (*31*). The participation of surface and lattice oxygen creates anisotropic displacement of the ligation to cobalt, causing an increase of 1s → 3d transition intensity. The Co XANES and EXAFS spectra were nearly fully restored to their original intensities at the onset voltage (1.23 V) when the cell potential was returned to 1.02 V, suggesting the reversibility of the active-site restructuring in LMCF. By contrast, XANES spectra at the Mn K-edge and La L_{III}-edges

show little changes under different cell potentials (Fig. 2, B and C). Compared with Co, the EXAFS spectrum of Mn only showed a minor reduction of shell peak intensity at 1.23 V after the catalyst was immersed in the electrolyte. No apparent changes in shell structure and DWF were observed for Mn during OER (Fig. 2E and fig. S13). XANES and EXAFS analyses indicate that Mn and La do not participate in the electrocatalysis directly. Rather, their presence modifies the structure and activity of the cobalt site. To this end, we also investigated the in situ XAS at different potentials over the fibrous cobalt oxide catalyst prepared by the same method but in the absence of Mn and La (CF). The changes in XANES and EXAFS are significantly less dominant than those found in LMCF (fig. S28).

Comparison with theory

The experimentally observed atomic and electronic configurations in LMCF correspond well with density functional theory (DFT)
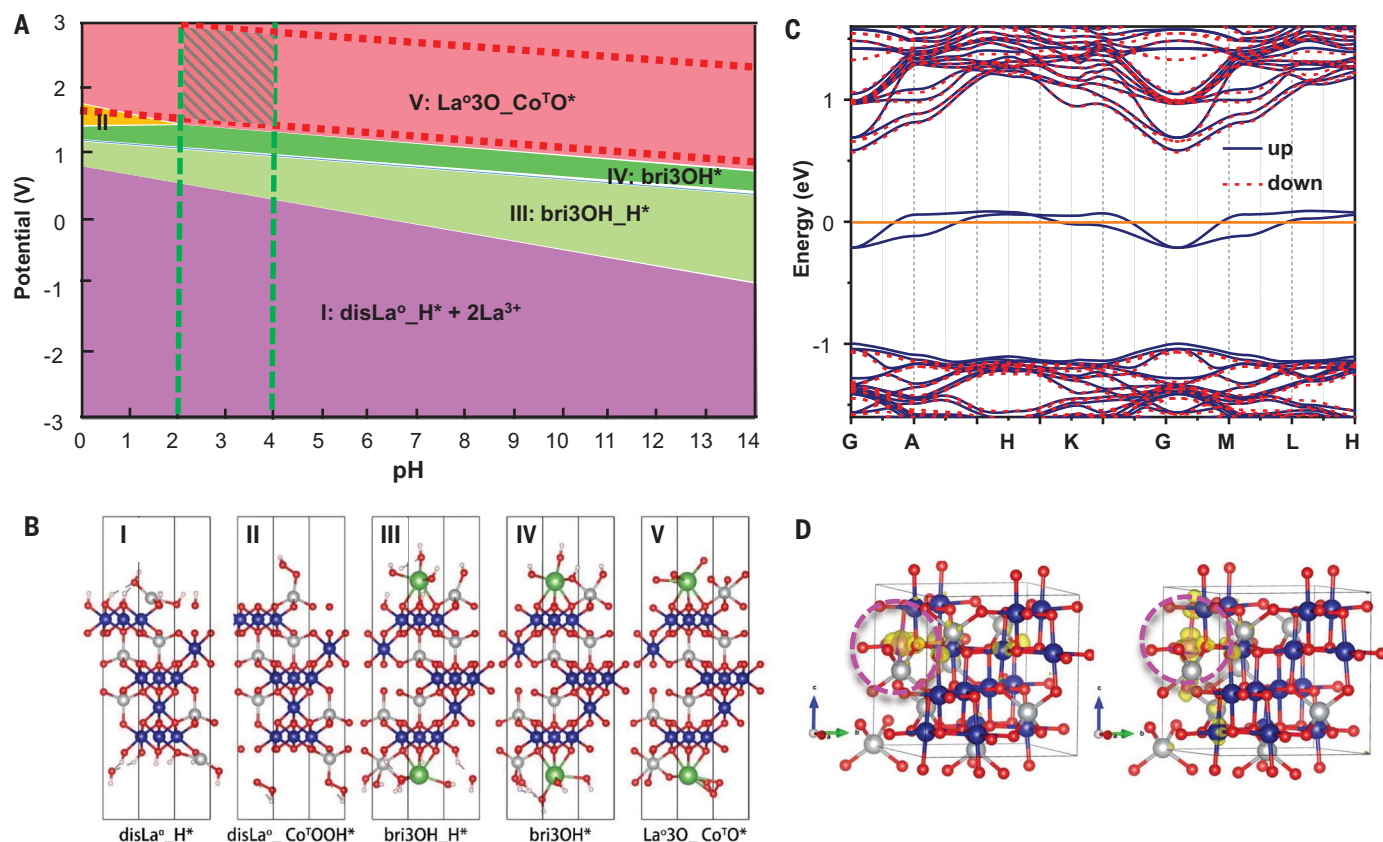
Fig. 4. Computational Pourbaix diagram and Fermi band structure of LMCF. (**A**) Surface Pourbaix diagram for the La-doped Co_3O_4 (111) facet obtained from the DFT + U calculations. (**B**) Possible intermediate state configurations. Blue, gray, red, and white balls denote the octahedral Co^{3+}, tetrahedral Co^{2+}, oxygen, and hydrogen ions. An asterisk denotes the pure surface; H* and _H* denote the configurations in which the surface oxygen atoms are covered by H; Co^O denotes the octahedral coordinated cobalt, and Co^T denotes the tetrahedral coordinated cobalt; the nO/nOH/nOOH refer to the numbers of O/OH/OOH groups covering over each Co atom; configurations denoted

"disCo/La" are generated after the Co/La dissolution; and the prefix "bri-" means that the covered groups act as a bridge connecting La^O and Co^T. The potential is relative to the standard hydrogen electrode (SHE). (**C**) Calculated Fermi band structure of LMCF by replacing Co^{3+} with Mn^{3+} in the Co_3O_4 lattice. (**D**) Charge density distribution at the Fermi level upon Mn substitution in LMCF. Yellow refers to the charge density contour. Blue, gray, and red balls indicate octahedral Co^{3+}, tetrahedral Co^{2+}, and oxygen, respectively. Mn ions are behind yellow contour and circled by violet dotted line.

calculations. For example, our calculation reveals that in the bulk, in terms of total energy, both Mn and La preferentially replace Co in octahedral rather than tetrahedral sites, with stability differences of 0.25 eV and 1.28 eV, respectively. This is in agreement with the above XAS observation of the increased Co^{2+} percentage due to the Mn and La doping. The stronger preference for La is because of its most stable +3 oxidation state, whereas Mn could be present in either a +2 or +3 state. Our calculation also shows that Mn preferentially remains in the bulk of the Co_3O_4, whereas La is extruded to the surface because of its large size. We compared the relaxed atomic structures of Mn and La at the surface layers and in the bulk of Co_3O_4 (fig. S29). For Mn, the surface layer structure is merely 0.1 eV higher than that in the bulk, suggesting that it can displace Co anywhere in the system. For La, the energy is 3.09 eV lower at the surface than in the bulk. This agrees well with the STEM measurement of Mn and La distributions, as shown in Fig. 1, G and H, affirming their roles as dopants in enhancing oxide conductivity and surface defect or oxygen vacancies for better OER activity according to our design concept (32).

For cobalt spinel–based OER catalysts operable in a PEMWE, the most imposing challenge is stability in the acidic media. To better understand the enhanced acid tolerance of LMCF under electrolytic condition, we calculated the surface Pourbaix diagram of the La-decorated Co_3O_4 (111) facet (Fig. 4A) because it represents the dominant facet in the LMCF observed by STEM (Fig. 1, F, G, and I, and fig. S6, D and E). The Pourbaix diagram consists of five regions—I: $disLa^o\_H^*$ + $2La^{3+}$, II: $disLa^o\_Co^TOOH^*$ + $2La^{3+}$, III: $bri3OH\_H^*$, IV: $bri3OH^*$, and V: $La^o3O\_Co^TO^*$—with their intermediate state configuration shown in Fig. 4B. Among these five phases, phases I and II contain ionic La^{3+} and therefore are unstable and soluble, whereas phases III, IV, and V contain the surfaces of Co^{2+}, Co^{3+}, and La^{3+} bridged by OH^*, OH_H^*, and O^* and exhibit relative stability against Co dissolution. Under low pH and low or negative potential, the surface La in the La-doped Co_3O_4 (111) facet dissolves to form La^{3+} (phase I). At potentials between 0.86 V and 1.1 V (RHE), the cation on the surface is oxidized and stabilized by OH^*, and the oxygen on the surface is covered by H^* to form the stable $bri3OH\_H^*$ structure (phase III). As the potential further increases to ≥1.23 V (RHE), the surface is protected by OH^* to form a $bri3OH^*$ stable structure (phase IV). Under high pH and high potential, the surface of the La-doped Co_3O_4 (111) facet tends to be oxidized by water, and the surface cations La and Co are protected by O^* by forming a stable structure $La^o3O\_Co^TO^*$ (phase V).

The calculated Pourbaix diagram demonstrates that the stability of the LMCF catalyst is defined by the combination of cell potential and pH. It also agrees well with our experimental observations. For example, under no electric field (potential = 0) at pH < 7, the catalyst is in phase I and is thermodynamically unstable in the acidic solution. During our RDE study in 0.1 M $HClO_4$ (pH = 1) at cell potentials between 1.5 V and 2 V, only a very small fraction of tests at low cell potential will overlap with phase II, which could explain why the dissolution rate was higher in the RDE test. In our PEMWE test, the actual cell voltage runs from 1.5 V to 3.0 V (between the two red dashed lines) within the anodic pH between 2 and 4 (defined by the two vertical green dashed lines) in Fig. 4A. Therefore, the actual PEMWE anode operates in a window within these two boundaries, as marked by the area covered by the green diagonal stripes. This operating window falls within phase V, $La^o3O\_Co^TO^*$, which is stable, thus offering a preliminary explanation of the stability of the LMCF catalyst in the PEMWE.

For comparison, we also calculated the Pourbaix diagram of the pure Co_3O_4 (111) facet and confirmed its weaker stability compared with the La-doped surface (fig. S30). We furthermore calculated Pourbaix diagrams of the LMCF (110) facet (fig. S31) and (100) facet (fig. S32). Both facets offer good stability under PEMWE operating conditions according to the calculation. Our study revealed the critical role of surface La in stabilizing multiple Co_3O_4 facets against corrosion under working PEMWE condition.

Another critical issue in electrocatalysis is the inherent electron conductivity of the oxide itself. Our calculation of LMCF shows that substituting a low concentration of Co^{3+} ions with uniformly distributed Mn^{3+} ions in the Co_3O_4 lattice induces two partially occupied defect states in the midbandgap (Fig. 4, C and D). The Mn-induced electron wave function overlaps significantly with neighboring Co ions, causing obvious dispersion and hence good electron mobility. This provides a direct enhancement of bulk-based electron conductivity, which, combined with the connectivity of the nanofibrous oxide network, offers an overall high conductivity value for LMCF. The improved electronic conductivity was further confirmed experimentally by the four-probe van der Pauw method (fig. S9).

Outlook

This study offers prospective directions and design insight for the future development of PGM-free OER catalysts for hydrogen production using PEMWE technology. For example, the catalytic activity enhancement can be further explored by increasing the surface functional group density through elemental doping,

primary size control, and morphology innovation. The PEMWE durability can be improved by removing the electrochemically unattached oxide, therefore limiting metal ion dissolution because of the lack of electro-potential stabilization. Fundamental understanding of the OER mechanism with respect to mononuclear versus binuclear reaction intermediates and catalytic pathways will help to guide the precursor and catalyst designs for lower overpotential and better acid tolerance (33, 34). These improvements offer paths to the next-generation, PGM-free OER catalysts as viable replacements for precious metals, such as iridium.

REFERENCES AND NOTES

1. K. Ayers et al., *Annu. Rev. Chem. Biomol. Eng.* **10**, 219–239 (2019).
2. M. Carmo, D. L. Fritz, J. Mergel, D. Stolten, *Int. J. Hydrogen Energy* **38**, 4901–4934 (2013).
3. M. T. M. Koper, *J. Electroanal. Chem.* **660**, 254–260 (2011).
4. R. D. L. Smith et al., *Science* **340**, 60–63 (2013).
5. B. Zhang et al., *Science* **352**, 333–337 (2016).
6. Z.-F. Huang et al., *Nat. Energy* **4**, 329–338 (2019).
7. T. Reier, H. N. Nong, D. Teschner, R. Schlögl, P. Strasser, *Adv. Energy Mater.* **7**, 1601275 (2017).
8. Z. W. Seh et al., *Science* **355**, eaad4998 (2017).
9. V. Artero, M. Chavarot-Kerlidou, M. Fontecave, *Angew. Chem. Int. Ed.* **50**, 7238–7266 (2011).
10. M. W. Kanan, D. G. Nocera, *Science* **321**, 1072–1075 (2008).
11. J. B. Gerken et al., *J. Am. Chem. Soc.* **133**, 14431–14442 (2011).
12. J. S. Mondschein et al., *Chem. Mater.* **29**, 950–957 (2017).
13. B. Rodríguez-García et al., *Sustain. Energy Fuels* **2**, 589–597 (2018).
14. N. Chatti et al., *Nat. Catal.* **2**, 457–465 (2019).
15. I. A. Moreno-Hernandez et al., *Energy Environ. Sci.* **10**, 2103–2108 (2017).
16. M. Blasco-Ahicart, J. Soriano-López, J. J. Carbó, J. M. Poblet, J. R. Galan-Mascaros, *Nat. Chem.* **10**, 24–30 (2018).
17. J. Bao et al., *Angew. Chem. Int. Ed.* **54**, 7399–7404 (2015).
18. S. L. Zhang et al., *Adv. Mater.* **32**, 2002235 (2020).
19. J. Shui, C. Chen, L. Grabstanowicz, D. Zhao, D. J. Liu, *Proc. Natl. Acad. Sci. U.S.A.* **112**, 10629–10634 (2015).
20. W. Wang, A. Janotti, C. G. Van de Walle, *J. Mater. Chem. C* **4**, 6641–6648 (2016).
21. Y. Wang et al., *Adv. Energy Mater.* **4**, 1400696 (2014).
22. Z. Morgan Chan et al., *Proc. Natl. Acad. Sci. U.S.A.* **115**, E5261–E5268 (2018).
23. L. C. Seitz et al., *Science* **353**, 1011–1014 (2016).
24. C. C. McCrory et al., *J. Am. Chem. Soc.* **137**, 4347–4357 (2015).
25. S. Geiger et al., *Nat. Catal.* **1**, 508–515 (2018).
26. Y. T. Kim et al., *Nat. Commun.* **8**, 1449 (2017).
27. C. H. van Oversteeg, H. Q. Doan, F. M. de Groot, T. Cuk, *Chem. Soc. Rev.* **46**, 102–125 (2017).
28. H. N. Nong et al., *Nat. Catal.* **1**, 841–851 (2018).
29. H. Dau, P. Liebisch, M. Haumann, *Anal. Bioanal. Chem.* **376**, 562–583 (2003).
30. M. Risch et al., *Energy Environ. Sci.* **8**, 661–674 (2015).
31. A. Grimaud et al., *Nat. Chem.* **9**, 457–465 (2017).
32. O. Diaz-Morales et al., *Nat. Commun.* **7**, 12363 (2016).
33. I. C. Man et al., *ChemCatChem* **3**, 1159–1165 (2011).
34. M. Busch, *Curr. Opin. Electrochem.* **9**, 278–284 (2018).
35. W. Xu et al., La and Mn-doped cobalt spinel oxygen evolution catalyst for proton exchange membrane electrolysis, dataset, Dryad (2023); https://doi.org/10.5061/dryad.76hdr7t1v.

SUPPLEMENTARY MATERIALS

science.org/doi/10.1126/science.ade1499
Materials and Methods
Figs. S1 to S32
Tables S1 to S8
References (36–70)